Rock Mechanics Bulletin 5 (2026) 100243

Contents lists available at ScienceDirect

Rock Mechanics Bulletin

journal homepage: www.keaipublishing.com/en/journals/rock-mechanics-bulletin

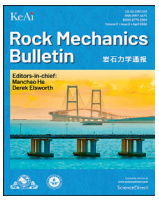

Full Length Article

Investigation of shale fracture behavior with different bedding properties based on discrete element method

Dubo Wang[a,b], Jinyu Dong[a,b], Dongqiao Liu[d], Xiangjun Chen[g], Hai Zhong[e], Mijia Yang[f], Hongjian Wang[a,b,c,*]

[a] North China University of Water Resources and Electric Power, Zhengzhou, 450045, China
[b] Henan Key Laboratory of Geological Environment Intelligent Monitoring and Disaster Prevention, Zhengzhou, 450045, China
[c] State Key Laboratory of Intelligent Coal Mining and Strata Control, Beijing, 100020, China
[d] State Key Laboratory for Tunnel Engineering, China University of Mining and Technology, Beijing, 100083, China
[e] School of civil Engineering, Sanming University, Sanming, 365004, China
[f] Construction and Environmental Engineering, North Dakota State University, Fargo, ND, 58108, USA
[g] Henan Polytechnic University, Jiaozuo, 454003, China

ARTICLE INFO

Keywords:
Shale
Interaction
Fracture diversion distance
Discrete element method (DEM)
Semi-circular bend (SCB) test

ABSTRACT

The interaction between cemented laminae and induced fractures plays a critical role in hydraulic fracture propagation within laminated shale reservoirs. By combining mode-I fracture mechanics experiment conducted on semi-circular bend (SCB) specimens of black carbonaceous shale from the marine Longmaxi Formation with numerical simulations, this study systematically investigates the effects of three key geological parameters: (1) bond strength, (2) vein stiffness, and (3) approach angle on fracture propagation characteristics. The key findings are summarized as follows: (1) Increasing the parallel bond strength promotes fracture crossing behavior. When the vein fracture toughness was reduced to 0.3, 0.2, and 0.1 times that of the shale matrix, fractures exhibited increased deflection tendency along the vein, creating longer stepped propagation paths. (2) For stiffer veins, induced fracture divert into the vein and propagate over longer distances; Additionally, more micro-cracks form within the vein before fracture-vein interaction occurs. (3) Fracture-vein interaction exhibits significant angular dependence: At approach angles between 60° and 90°, fractures predominantly penetrated laminae without deflection; Below 60°, fractures initially diverted into the vein but subsequently re-entered the matrix before reaching the vein terminus. This bifurcation pattern closely resembles laboratory observations of weakly cemented or pre-damaged vein specimens.

1. Introduction

Hydraulic fracturing (or hydro-fracturing) involves injecting highly pressurized fluid into the formations to create fractures, thereby enhancing production from low-permeability reservoirs (Wang et al., 2017). Pre-existing natural fractures (NFs) play a crucial role in the economic assessment of prospective formations (Kolawole et al., 2020). The interaction between hydraulic fractures (HFs) and natural fractures (NFs) in unconventional reservoirs, geothermal systems, and mining is a complex and largely unexplored process (Wu and Olson, 2014; Mteiri et al., 2021; Caox et al., 2022; He et al., 2015). Micro-seismic monitoring conducted in formations such as the Barnett Shale reveals extensive areas of disturbance during hydraulic fracture treatments, spanning hundreds of feet in width and extending up to a thousand or more feet in length (Fisher et al., 2005; Lin et al., 2024a,b). These diagnostic observations suggest that fracture propagation in shale and naturally fractured formations manifests as complex multi-fracture network growth rather than the extension of discrete planar fractures (Maxwell et al., 2002). Empirical evidence supports the hypothesis that pre-existing natural fractures provide preferential pathways for hydraulic fracture redirection (Gale et al., 2007, 2014). The fracture interaction mechanism is fundamental for creating the enhanced permeability networks necessary for economically viable production in ultra-low permeability shale formations (Osiptsov, 2017).

* Corresponding author.
E-mail address: wanghj@ncwu.edu.cn (H. Wang).

Peer review under the responsibility of Chinese Society for Rock Mechanics & Engineering.

https://doi.org/10.1016/j.rockmb.2025.100243
Received 26 February 2025; Received in revised form 18 July 2025; Accepted 8 August 2025
Available online 6 September 2025

Previous studies on hydraulic fracture-natural fracture interactions have predominantly focused on frictional interfaces: discontinuities exhibiting shear resistance but negligible tensile strength (Gao et al., 2024). Experimental and theoretical analyses have demonstrated that three critical parameters govern hydraulic fracture behavior at pre-existing discontinuities: (1) approach angle, (2) interfacial friction coefficient, and (3) horizontal differential stress parallel to the hydraulic fracture propagation direction, which collectively determine whether fractures arrest, divert into, or cross natural fractures (Renshaw and Pollard, 1995). The natural fractures modeled in these studies typically represent either uncemented joints in geological formations or artificially created unbonded interfaces produced in hydrostone (gypsum-based analog material) using mechanical saw-cutting techniques. While unmineralized fractures dominate surface exposures, subsurface core analyses from hydrocarbon reservoirs, particularly the Barnett Shale, reveal that most natural fractures exhibit partial to complete cementation (Laubach, 2003; He et al., 2022a,b,c). International research efforts have systematically investigated hydraulic-natural fracture interactions, establishing fundamental predictive criteria such as Blanton's stress contrast principle (Blanton, 1982), Warpinski and Teufel's energy balance framework (Warpinski and Teufel, 1987), Renshaw's critical stress ratio (Renshaw and Pollard, 1995). These theoretical frameworks have been validated through extensive experimental and numerical studies (Wu et al., 2012; Chuprakov et al., 2011; 2013). Subsequent research has extended these models to predict final fracture network morphology under interaction scenarios (Zhang et al., 2007; Damjanac and Cundall, 2016). However, as these models incorporate increasingly complex considerations, computational simulations become more complicated with reduced practical applicability.

Fracture toughness, a critical mechanical property governing rock deformation behavior, plays a pivotal role in evaluating three fundamental aspects of geomechanical systems: intrinsic rock strength, crack initiation/propagation mechanisms, and macroscopic fracture pattern development (Atkinson, 1989; Wang et al., 2016). This critical parameter necessitates standardized testing protocols and advanced numerical modeling approaches to accurately capture rock failure behavior under complex loading conditions. Significant progress has been made in developing computational frameworks that replicate realistic rock deformation and failure processes. Current numerical strategies can be primarily categorized into two methodological paradigms: 1) Continuum-based approaches incorporating damage mechanics principles, where inelastic deformation is modeled through progressive degradation of constitutive relationships (Wang et al., 2004; Du et al., 2022); and 2) Discrete fracture modeling techniques that explicitly represent crack evolution, exemplified by the Discrete Element Method (DEM), a particle-based computational framework for simulating discontinuous media (Potyondy and Cundall, 2004; Itasca Consulting Group Inc, 2015). For example, Gao et al. (2020, 2024) employed PFC to investigate the influence of structural planes on the meso-scale mechanical behavior of rocks; while utilized PFC to examine the shear behavior and dilatation of bimrocks featuring rock-like matrices, such as conglomerates.

This study employs a coupled experimental-computational approach to investigate fracture interaction mechanisms in veined shale formations, with particular focus on interpreting the micromechanical origins of hydraulic fracture complexity observed in the Longmaxi Formation shale experiments by Wang et al. (2017). Through DEM modeling calibrated with laboratory data, we systematically analyze the interactions between induced tensile fractures and calcite-filled veins of varying thicknesses, in Longmaxi shale specimens under semi-circular bend (SCB) loading conditions. The research specifically addresses three critical geomechanical parameters governing fracture-vein interactions: Approach angle between propagating fractures and vein orientation, Mechanical strength contrast at shale-vein interfaces, Stiffness differential between host rock and mineralized veins. These parameters collectively determine the dominant interaction mode: fracture arrest, direct crossing, or path diversion-with direct implications for predicting fracture network complexity in shale reservoirs.

2. Specimen preparation and experimental tests

2.1. Specimen preparation

The shale samples were collected from Shizhu County, Chongqing, China, where outcrops occur at approximately 1520 m above sea level. These rocks were identified as black carbonaceous shale from Lower Silurian Longmaxi Formation, characterized by bedding joints and well-developed networked micro-fractures. Fig. 1 shows the outcrop shale with layered joints at the Da Fengao of Shizhu County, Chongqing. Analysis of fractured shale fragments indicates high mud content, high brittleness, and low hardness.

The schematic diagram of the v-shaped groove is shown in Fig. 2. The V-shaped groove is processed by a diamond wire cutting machine, which can realize a prefabricated artificial seam with a width of 0.5 mm. When calculating the K_{IC} value, the stress distribution at the tip of the fine groove is closer to that of the sharp crack. In addition, the flatness and verticality of the cutting surface are also better than that of diamond thin blade sewing, which can ensure that the two wings of the linear groove are in a vertical plane and are symmetrical with each other. It is necessary to place a wedge-shaped pad at the angle of θ at the bottom of the specimen, and set the stroke H_c in the vertical direction of the cutting line (calculated by the trigonometric function) to form a beveled groove at the angle of θ. During the line cutting operation, the cutting part needs to be water-cooled to prevent friction and thermal erosion from changing the fracture toughness of the rock cutting joint.

A MTS-CMT5105 testing machine with the maximum loading force of 100 kN is controlled by the visualized operating software on Windows platform, as shown in Fig. 3a. It can record the current load, displacement, stress and strain, and plot corresponded curves simultaneously. According to the ISRM suggested method for testing rock fracture toughness, SCB specimens were prepared from shale cores (ISRM, 1988; 1995; Wang et al., 2016; Zhao et al., 2021). The straight notches of SCB specimens were cut by diamond saws with thickness of 1.2 mm. The geometrical configuration is shown in Fig. 3b, and the suggested geometrical dimensions of standard specimen are presented in Table 1. In Fig. 3b, R, a and B indicate the radius of specimen, the crack length and the thickness of the notch, respectively. Moreover, s is the distance between the two supporting cylindrical rollers and P is actually the monotonically increasing compressive load applied at the central loading roller of the three-point bend loading.

2.2. Sample properties

Howarth and Rowlands (1987) noted that rock mass structure and composition are essential factors influencing mechanical properties. The structure of rock mass includes particle shape, particle distribution orientation, particle boundaries, and interparticle bonding. The composition of rock mass mainly includes mineral types, particle components and interparticle cements. Barton et al. (1985) demonstrated that joints strength variations are the primary cause of specimen failure strength disparity. Bell and Lindsay (1999) established that the increasing clay mineral content reduces uniaxial compressive strength (UCS) in sandstone, whereas quartz content increases uniaxial compressive strength of rock mass.Joint strength characteristics can be analyzed from two extreme aspects: the joint without filling is a fully developed crack, and the joint with filling is a structural plane with a certain strength. Studies indicate that under uniaxial compression, fractured rock mass containing fillings enjoys high peak strength, which backs up the cracking resistance of jointed rock mass (Kulatilake et al., 2001; Barton and Choubey, 1977). Filling material in joint is mostly mineral cementation surface, crack occurs initially on the weaker cementation surface among mineral particles, and the initial crack

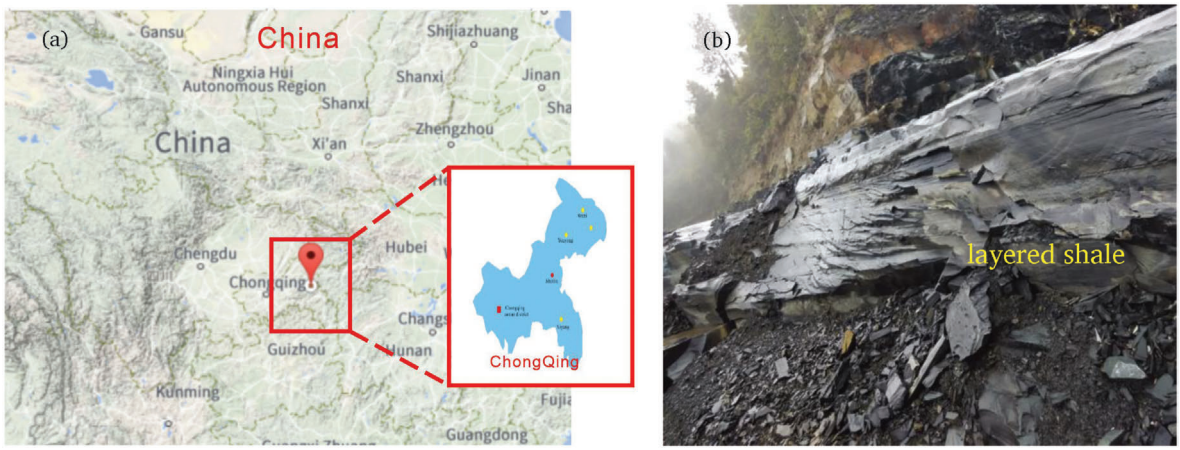

Fig. 1. Outcrop shale:(a) Location of the shale rock sample, (b) Outcrop shale with layered joints.

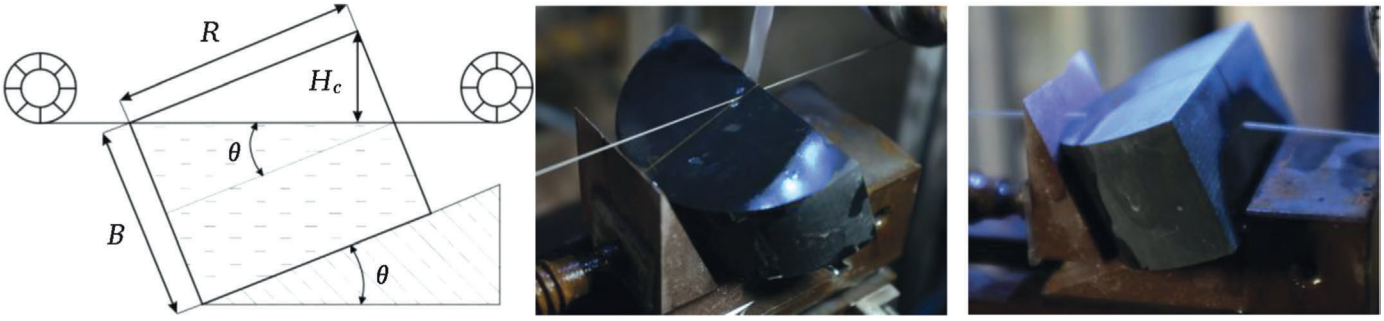

Fig. 2. Machining of SCB notch.

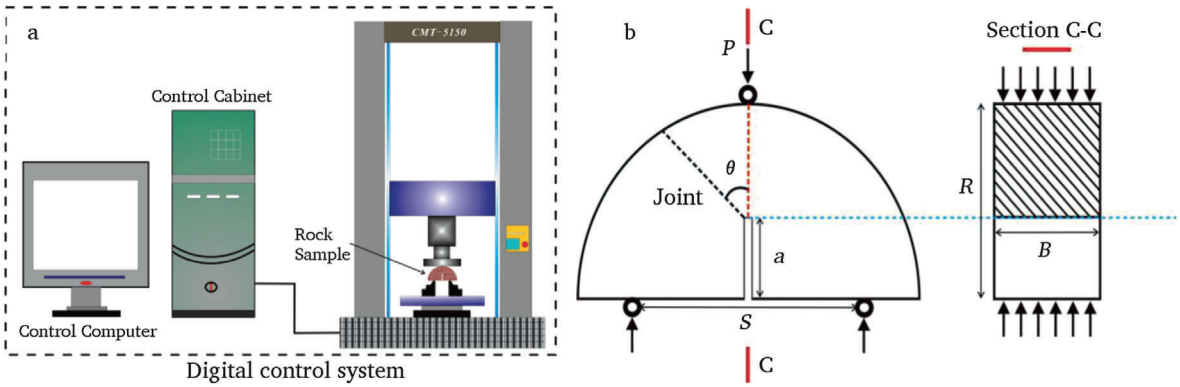

Fig. 3. Geometry of CCNBD and SCB specimens with loading arrangement: (a) MTS-CMT5105 testing machine and (b) SCB specimen (Wang et al., 2017).

Table 1
Standard SCB specimens geometrical dimensions.

Descriptions	Diameter (D)	Thickness (B)	Crack length (a)	Span length (s)
Values (mm)	Large of 10× grain size or 76 mm	Large of 0.4D or 30 mm	$0.4 \leq a/R \leq 0.6$	$0.5 \leq s/2R \leq 0.8$

propagation angle is mainly determined by the included angle among these mineral particles. Regarding cement strength: siliceous and ferruginous cements exhibit the highest strength, calcareous cements moderate strength, and argillaceous (clay-based) cements the lowest cohesive strength.

Based on prior characterization, the experimental sample comprise marine sedimentary black carboniferous shale from Longmaxi Formation. To investigate discontinuity and mineral composition effects on shale's fundamental mechanical properties, uniaxial compression tests were performed on specimens containing discontinuities at varying orientations, with post-failure X-ray mineralogical analysis conducted on newly exposed cementation surfaces. As shown in Table 1, the statistical results indicate that the highest mineral composition of the bonding surface is quartz, reaching 85%, followed by potassium feldspar and plagioclase, and the clay content comes the last, with an average value of 0.35%. Conversely, the clay in the mineral content of shale matrix is up to more than 50% while quartz turns out to be merely 20%.

2.3. Semi-circular bend test

Chong and Kuruppu (1984) propsoed the Semi-circular Bend (SCB) test as a standard method for measuring rock fracture toughness (Fig. 3b). This study employed 12 SCB specimens to test the Mode-I fracture toughness of shale. Texture direction angle θ was the angle between the loading direction and the bedding plane, which was 0°, 45° and 90° respectively. There were 4 specimens in each loading scheme. The geometric size of the specimen in this test was set as $D = 75$ mm; the thickness was larger than or equal to 0.4 times of the diameter, thus set $B = 30$ mm; the artificial slit length must meet the requirement of $0.4 \leq a/R = \beta \leq 0.6$, thus set $a = 16$ mm; the span of the supporting round rods was needed to make selected as $0.5 \leq \frac{s}{2R} \leq 0.8$, thus set $S = 60$ mm. Experiments were conducted using a servo-controlled testing system CMT 5105 with a digital controller. The loading rate applied on SCB specimens was set applied at a displacement rate of 0.06 mm/min for all the tests. Both the maximum failure loads and the load versus load point displacement (LPD) curves were recorded. Other suggested specifications for SCB tests were strictly adhered to.

The fracture toughness value of SCB can be calculated as follows (Kuruppu et al., 2015):

$$K_{SCB} = \frac{P\sqrt{\pi a}_{max}}{2BR'} \tag{1}$$

$$Y' = -1.297 + 9.516(s/2R) - (0.47 + 16.457(s/2R))\beta + (1.071 + 34.401(s/2R))\beta^2 \tag{2}$$

where a, R, and B are artificial notch length, radius, and thickness of the specimen, respectively; P_{max} is the maximum load and $\beta = a/R$; Eq. (2) gives the non-dimensional stress intensity factor derived using the finite element method while assuming plane-strain conditions. All the tested SCB data and statistical values are respectively listed in Table 3 (Wang et al., 2017).

3. Materials and numerical methods

3.1. Micro-parameters of shale

The Particle Flow Code (PFC), as a discrete element method (DEM) implementation, simulates granular systems through three fundamental components: particles, contacts, and constitutive models (Itasca Consulting Group Inc, 2015). As a discrete element method software, PFC's advantage lies in its ability to model rock materials using circular particles, enabling high-fidelity simulation of layered and heterogeneous materials. Moreover, interparticle contacts and their properties can be configured according to material characteristics. Additionally, it facilitates visual observation of rock failure processes, fracture type analysis, and quantification of crack networks, significantly advancing the understanding of rock fracture mechanisms (Tang et al., 2025). Particles: Discrete elements with defined mass and geometry representing mineral grains or composite aggregates; Bonds: Interparticle connections creating cohesive assemblies that mimic intact rock fabrics; Walls: Boundary entities with dual functions: (a) geometric constraints for specimen generation, and (b) loading surfaces for controlled deformation (Potyondy and Cundall, 2004). Potyondy's pioneering work established the Bonded-Particle Model (BPM) framework through PFC2D/3D implementations, systematically correlating microscale particle interactions with macroscopic rock behavior (Potyondy, 2015). The linear parallel bond model, a BPM variant, effectively captures the micromechanical response of cemented geological materials through two constitutive elements: Linear contact elements: Govern elastic interactions without rotational/tensile resistance; Parallel bond elements: Provide moment-resisting bonds that maintain connectivity until critical shear/tensile thresholds are exceeded (Wang et al., 2018).

To acquire appropriate microscopic parameters for the numerical model of the material, fundamental mechanical tests, which include uniaxial compression test and Brazil splitting test, were conducted. In the uniaxial compression test, a standard cylindrical specimen with a height of 100 mm and a radius of 50 mm was employed, whereas for the Brazil splitting test, a Brazilian disk specimen with a radius of 50 mm and a thickness of 25 mm was employed. These tests were performed on an TAW-2000 electro-hydraulic servo rock mechanic system to obtain stress-strain curves, uniaxial compressive strength σ_f/MPa, tensile strength σ_t/MPa, elastic modulus E and Poisson's ratio ν. These material properties from physical experiments are presented in Table 4. As shown in Figs. 4 and 5, the numerical results are compared with the laboratory test results from both the aspects of failure mode and mechanical test curves. After a series of repeated parameter adjustments by trial and error, the simulation results became consistent with the laboratory results, and the mesoscopic parameters of the numerical specimen are shown in Table 5. It can be seen that the simulated UCS, Young's modulus, tensile strength and Poisson's ratio of the intact rock specimen are similar or equal to those obtained from experiments. The main parameters include particle parameters of modulus (E), particle density (ρ), minimum particle radius (R_{min}), maximum particle radius (R_{max}), normal-to-shear stiffness ratio (k_n/k_s) and friction coefficient (μ) and parallel bond parameters of number of effective modulus (E_p), normal-to-shear stiffness ratio (k_n/k_s), tensile strength (σ_t), cohesion (c_p), and friction angle. The adopted loading rate of these PFC simulation tests was set as “0.6 mm/min”.

3.2. Numerical model by DEM

Fig. 6a presents the SCB specimen in the laboratory. According to the

Table 2
Mineral components of shale rock cemented plane (Wang et al., 2017).

Shale specimen/(Tendency)	Quartz/%	Potassium Feldspar/%	Plagioclase/%	Calcite/%	Clay/%
Parallel bedding plane	83.01	4.93	3.1	8.37	0.59
Inclined bedding plane	89.62	1.31	2.34	6.62	0.11
Vertical bedding plane	86.33	2.74	2.35	8.24	0.34
Average	86.32	2.99	2.60	7.74	0.35

Table 3
Mode-I fracture toughness values from all tested SCB specimens.

S.no.	B1	B2	B3	B4	D1	D2	D3	D4	F1	F2	F3	F4
Angle θ/°		0°				45°				90°		
P_{max}/N	1291	1238	932.7	-	984	1465	1645	1611	1638	1113	1611	1677
		1154 (average value)				1398 (average value)				1487 (average value)		
Y'	5.642	5.822	5.569	-	5.686	5.92	5.489	5.608	5.915	5.631	5.781	5.899
K_{IC}/(MPa·m1/2)	0.721	0.728	0.516	-	0.565	0.891	0.873	0.871	0.983	0.614	0.833	0.889
		0.655 (average value)				0.800 (average value)				0.830 (average value)		

Table 4
Comparison of material properties of physical experiment and numerical study.

	Uniaxial compressive strength σ_f/MPa	Tensile strength σ_t/MPa	Young's modulus E/GPa	Poisson's ratio ν
Physical experiment	146.43	4.54	23.66	0.193
PFC simulation	144.90	4.61	22.31	0.201

above mentioned model parameters, the numerical model of the SCB specimen was established, as shown in Fig. 6b. The notch at the bottom of the numerical sample was created by deleting the parallel bonds within the specified range. The specimen diameter is 75 mm and the initial notch length is 16 mm. The numerical sample consists of 34,355 particles and 83,250 parallel bonds. Dark gray particles represent shale matrix and yellow particles compose the calcite-cemented vein (see Fig. 6c). The out-of-plane thickness of the numerical model is 1 mm. Three cylindrical walls (one above and two below the specimen) represent the loading and supporting rollers, which apply a three-point bending force on the sample to generate an opening mode-I fracture from the tip of the notch. The support rollers are kept separated by a fixed span length of 60 mm, which is same as that used in the physical tests. Fig. 6d shows an amplified view of the shale matrix (dark gray) with a vein (yellow). The angle θ between the bedding plane and the vertical loading direction is 90°. The element size is defined as shown in Table 5. The particle size used for the sample constrained the minimum thickness of vein. In order to make the vein have independent properties from the shale matrix, its thickness should be at least two times of the maximum particle diameter ($2D_{max}$ = 0.4 mm). Otherwise, a vein particle could be bonded to matrix particles on both sides of the vein. Considering the variability of random packing and particle contacts, it was found that the achievable minimum vein thickness is 2.0 mm due to modeling constraints. The microscopic properties of the vein, the stiffness and strength of the parallel bonds and the stiffness of the particles, can be set as ratios of the corresponding rock matrix values.

3.3. Numerical simulation scheme

Dahi-Taleghani and Olson (2009) introduced the maximum energy release rate criterion for forecasting the fracture

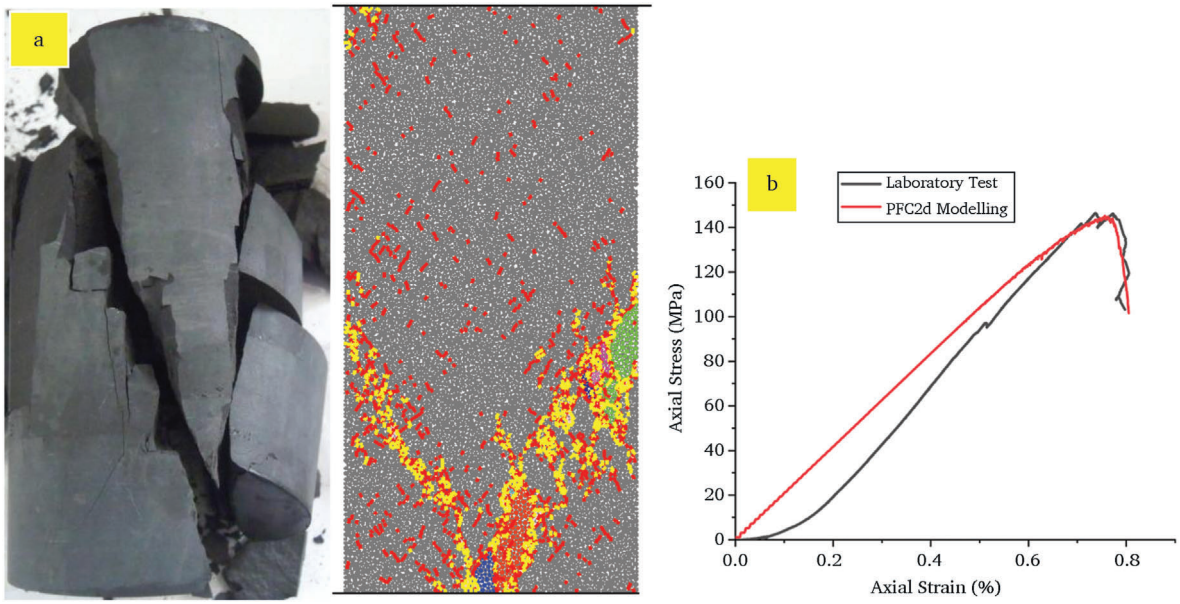

Fig. 4. Calibration of the parallel bond contact model to the laboratory sample under UCS test. (a) UCS test in simulation. (b) Comparison between experimental and numerical results.

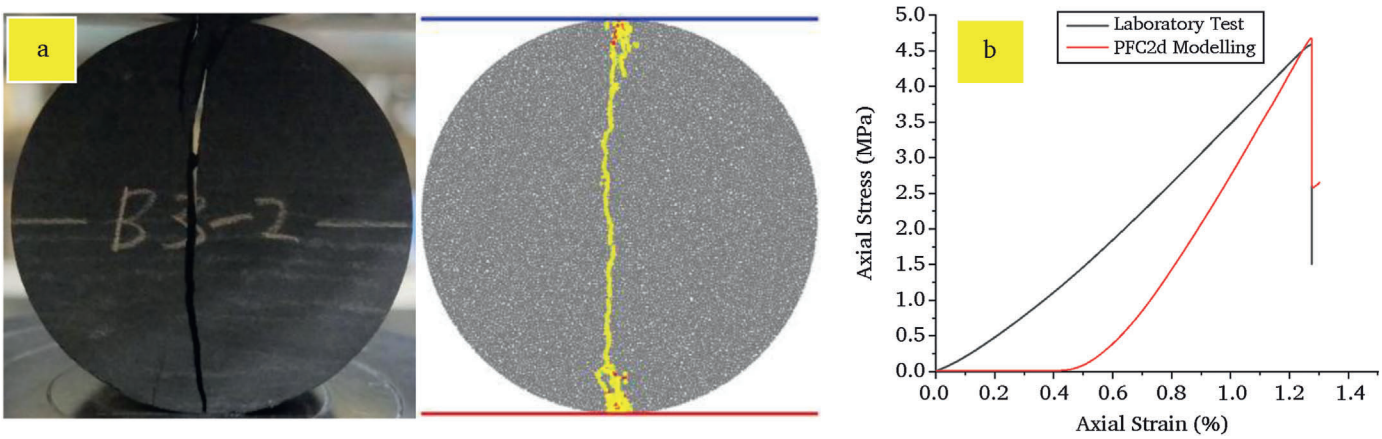

Fig. 5. Calibration of the parallel bond model to the laboratory sample under Brazilian test. (a) Tensile test in simulation. (b) Comparison between experimental and numerical results.

Table 5
Calibrated mesoscopic parameters of the parallel bond contact model.

Particle properties		Parallel bond properties	
Modulus, E (GPa)	50	Modulus, E_p (GPa)	50
Normal/Shear Stiffness Ratio, k_n/k_s	1.5	Normal/Shear Stiffness Ratio, $\bar{k}_n/\bar{k}_s$	1.5
Minimum Particle Diameter, D_{min} (mm)	0.25	Tension Strength, σ_t (MPa)	32
Maximum Particle Diameter, D_{max} (mm)	0.50	Cohesion, c_p (MPa)	35
Friction Coefficient, μ	0.7	Friction Angle, (°)	30
Density, ρ (kg/m^3)	2650		

crossing-versus-diversion behavior of hydraulic fractures when interacting with veins. A fracture propagates in the direction which the energy release rate (G) reaches the critical value of the rock (G_c^{rock}) or the vein (G_c^{vein}). The critical energy release rate is related to fracture toughness and stiffness written as (Lawn and Wilshaw, 1975):

$$G_C = \frac{(K_{IC})^2}{E^*} \tag{3}$$

where K_{IC} is the fracture toughness and $E^* = E/(1-\nu^2)$ is the plain strain modulus. The dependence of fracture toughness on parallel bond strength was assessed by conducting SCB tests, revealing that the estimated fracture toughness is directly proportional to the parallel bond strength (Hunjoo et al., 2018). The parallel bond strength of 32 MPa is the value calibrated with the mechanical properties of Longmaxi shale, and the fracture toughness of the Longmaxi shale in PFC2D is 0.83 MPa·m$^{1/2}$. In this study, the diversion distance ($x = x_1 + x_2$) indicate the fracture propagating distance along the vein, which develop between the initial intersection and the location where the fracture kinks back into the host rock, as shown in Fig. 7.

Table 6 provides the specific schemes of the numerical simulation experiment in our current study. Fig. 9d–i: With the approaching angle held constant at 90°, the influence of different vein strengths on cracks propagation through the layer was studied. Fig. 10d–i: With the approach angle held constant value at 45°, the influence of different texture stiffness on the cracks propagation through the layer is studied. Fig. 10d–i: With the strength ratio between vein and rock is 0.5 (G_C^{vein}/G_C^{rock} is 0.25), the influence of different approach angles on cracks propagation through the layer was studied.

4. Experimental results

4.1. Influence of vein strength on fracture path

To evaluate the impact of vein fracture toughness on the fracture interaction behavior, the vein parallel bond strength was varied while keeping all other properties constant ($\theta = 90°$, $w = 1$ mm, $1 \times E^{rock}$). With increasing parallel bond strength, fracture interaction tend to result in crossing, as shown in Fig. 8a (in the case of $K_{IC}^{vein}/K_{IC}^{rock} = 0.5$, $G_C^{vein}/G_C^{rock} = 0.25$). Overall, the weaker veins have greater impacts on the fracture propagation trajectory. As shown in Fig. 8b, with an approach angle of 90° (in the case of $K_{IC}^{vein}/K_{IC}^{rock} = 0.4$, $G_C^{vein}/G_C^{rock} = 0.16$), the induced fracture initially extends straight from the notch and crosses the vein, though there is a slight deflection from a

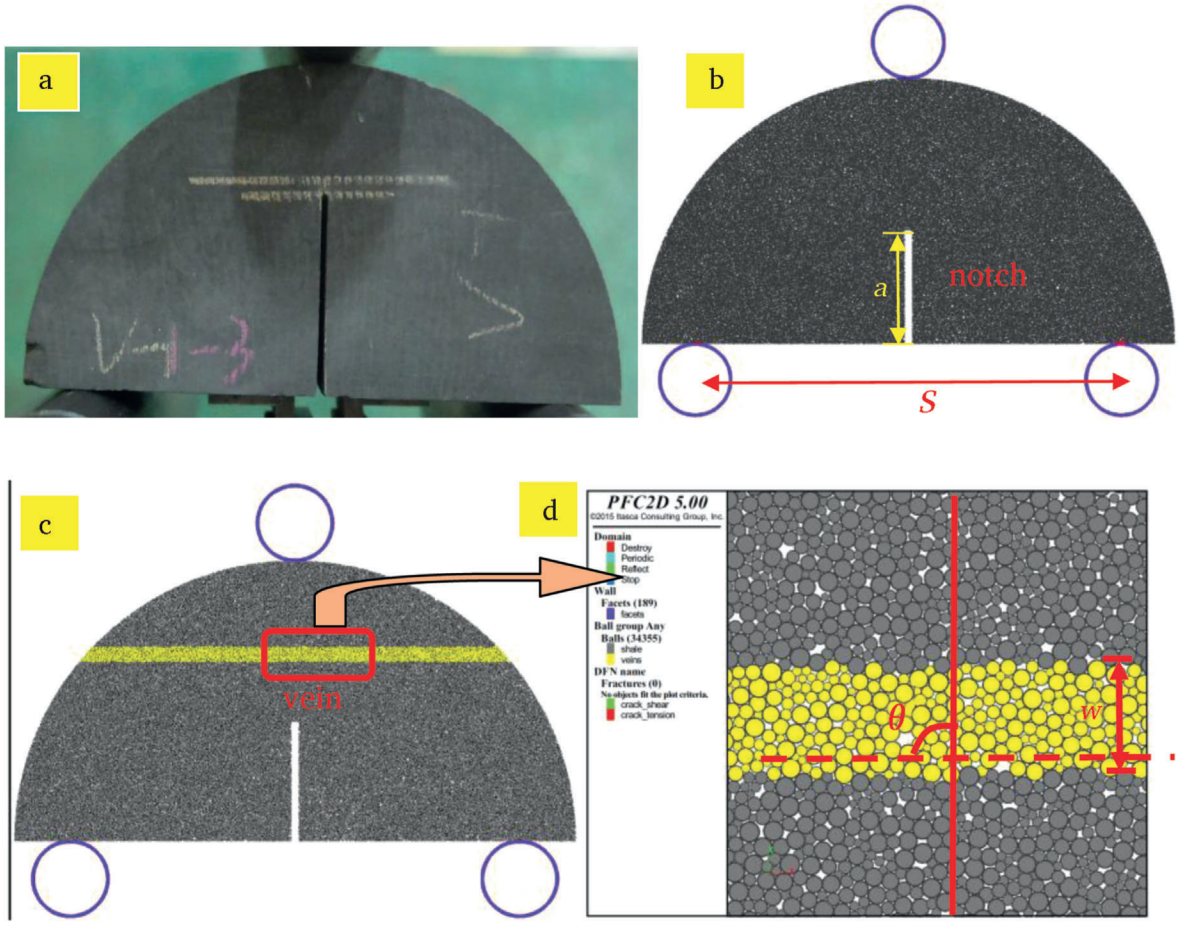

Fig. 6. Schematic views of SCB numerical test set-up: (a) SCB Shale specimen, (b) Particle discrete element model of SCB specimen, (c) Numerical model of SCB speicmen with a 90° vein (particles in yellow color), and (d) Magnified view of shale matrix (dark gray particles) with a vein (yellow particles).

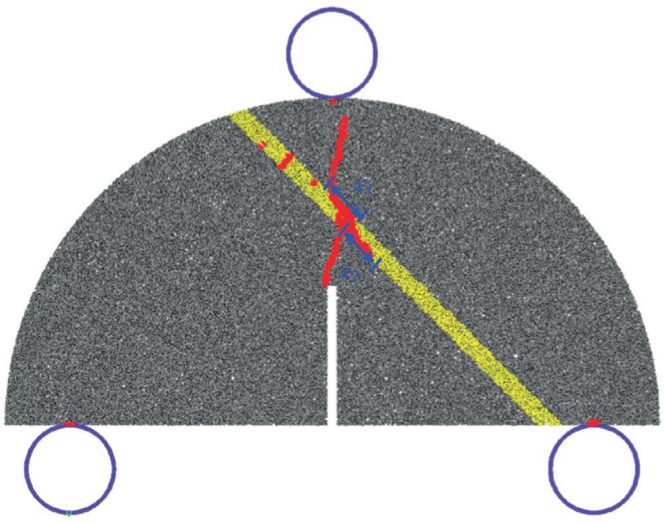

Fig. 7. The SCB numerical test result using PFC2D with measurements of fracture diversion distance (x_1 and x_2).

planar path near the vein itself. Through reducing the vein fracture toughness to a lower value, approximately 0.3, 0.2 and 0.1 times of the shale fracture toughness which means the ratios of G_C^{vein}/G_C^{rock} are 0.09, 0.04, 0.01 respectively, the opening mode fracture tends to divert and propagate a longer distance along the vein, generating a longer step (see Fig. 8c–e).

Fig. 9 shows the influence of vein strength on the fracture diversion distance and the number of fracture. It is evident from the figure that when the vein strength increases, both diversion distance and the number of fracture decrease gradually. When $K_{IC}^{vein}/K_{IC}^{rock} = 0.1$, the total distance of fracture deflection is 46.03 mm, and the number of new micro-fractures reaches 1243. When $K_{IC}^{vein}/K_{IC}^{rock} = 0.5$, there generate only 113 micro-fractures with the total length of deflection distance merely of 1.14 mm. Based on this investigation of vein strength effects on fracture propagation, it can be inferred that during in-situ hydraulic fracturing for reservoir interlayer reconstruction, the interlayer should exceed 50% of the target rock layer strength. Otherwise, the newly generated fractures shall mainly expand in the interlayer, and the targeted reservoir cannot be fractured by hydraulic fracturing, thus failing to achieve the goal of increasing production and efficiency.

4.2. Influence of vein stiffness on fracture path

An important aspect of the energy release rate criterion involves considering vein stiffness (E^{*vein}) in estimating the critical energy release rate (see Eq. (3)). Such considerations are generally neglected in other fracture interaction analyses (Wang et al., 2017; Amir et al., 2024). Hence, to investigate whether vein stiffness controls the vein's behavior as a plane of weakness in the fracture-interaction process, the second group comprises nine samples all containing a vein with $\theta = 45°$, and a constant parallel bond strength ($0.5 \times K_{IC}^{rock}$), but different vein stiffness E^{*vein} ($0.5 \times E^{*rock}$, $1.0 \times E^{*rock}$, $1.5 \times E^{*rock}$, $2.0 \times E^{*rock}$, $2.5 \times E^{*rock}$, $3.0 \times E^{*rock}$, $3.5 \times E^{*rock}$, $4.0 \times E^{*rock}$, $5.0 \times E^{*rock}$). Then, the corresponding vein critical energy release rate (G_C^{vein}) can be calculated from Eq. (3), which are $0.5 \times G_C^{rock}$, $0.25 \times G_C^{rock}$, $0.17 \times G_C^{rock}$, $0.13 \times G_C^{rock}$, $0.10 \times G_C^{rock}$, $0.08 \times G_C^{rock}$, $0.07 \times G_C^{rock}$, $0.06 \times G_C^{rock}$ and $0.5 \times G_C^{rock}$, respectively.

When the vein stiffness is 0.5, 1 and 1.5 times of the shale stiffness, all of the induced fractures in Fig. 10a and b and c cross the vein directly; When the vein stiffness is 2–5 times the shale stiffness,the induced fractures as shown in Fig. 10d–i, first divert into the vein but subsequently kink back into the rock matrix before propagating to the end of the vein. As the vein stiffness increases, the induced fracture develops a longer diversion distance. That's because there generates higher stress in the vein with higher E^{*vein} than that in the shale, which causes the vein to act more like a weaker plane. Furthermore, for the case of $E^{*vein} = 5.0 \times E^{*rock}$ (see Fig. 10i), numerical specimen occurs failure

Table 6
Experimental Scheme on Numerical Simulation

Scheme	Samples No	Shale								
		E_{mod} /(Gpa)			pb_ten/(MPa)		pb_coh/(MPa)	pb_fa/(°)	K_{IC}^{rock}/(MPa·m1/2)	G_C^{rock}/(N/m)
		50			32		35	30	0.83	13.22
		Veins								
		Approach angle (°)	E^{vein}/E^{rock}	E^{vein}/(Gpa)	**pb_ten**		**pb_coh**	**pb_fa/(°)**	$K_{IC}^{vein}/K_{IC}^{rock}$	G_C^{vein}/G_C^{rock}
					Strength ratio (vein / rock)	**value**				
I	SCB-load-0	90	1	50	0.1	3.2	35	30	0.1	0.01
	SCB-load-0-1	90	1	50	0.2	6.4	35	30	0.2	0.04
	SCB-load-0-2	90	1	50	0.3	9.6	35	30	0.3	0.09
	SCB-load-0-3	90	1	50	0.4	12.8	35	30	0.4	0.16
	SCB-load-0-4	90	1	50	0.5	16.0	35	30	0.5	0.25
II	SCB-E-1	45	0.5	25	0.5	16.0	35	30	0.5	0.5
	SCB-E-2	45	1	50	0.5	16.0	35	30	0.5	0.25
	SCB-E-3	45	1.5	75	0.5	16.0	35	30	0.5	0.17
	SCB-E-4	45	2	100	0.5	16.0	35	30	0.5	0.13
	SCB-E-5	45	2.5	125	0.5	16.0	35	30	0.5	0.10
	SCB-E-6	45	3	150	0.5	16.0	35	30	0.5	0.08
	SCB-E-7	45	3.5	175	0.5	16.0	35	30	0.5	0.07
	SCB-E-8	45	4	200	0.5	16.0	35	30	0.5	0.06
	SCB-E-9	45	5	250	0.5	16.0	35	30	0.5	0.05
III	SCB-0.5-15	15	1	50	0.5	16.0	35	30	0.5	0.25
	SCB-0.5-30	30	1	50	0.5	16.0	35	30	0.5	0.25
	SCB-0.5-45	45	1	50	0.5	16.0	35	30	0.5	0.25
	SCB-0.5-60	60	1	50	0.5	16.0	35	30	0.5	0.25
	SCB-0.5-75	75	1	50	0.5	16.0	35	30	0.5	0.25
	SCB-0.5-90	90	1	50	0.5	16.0	35	30	0.5	0.25

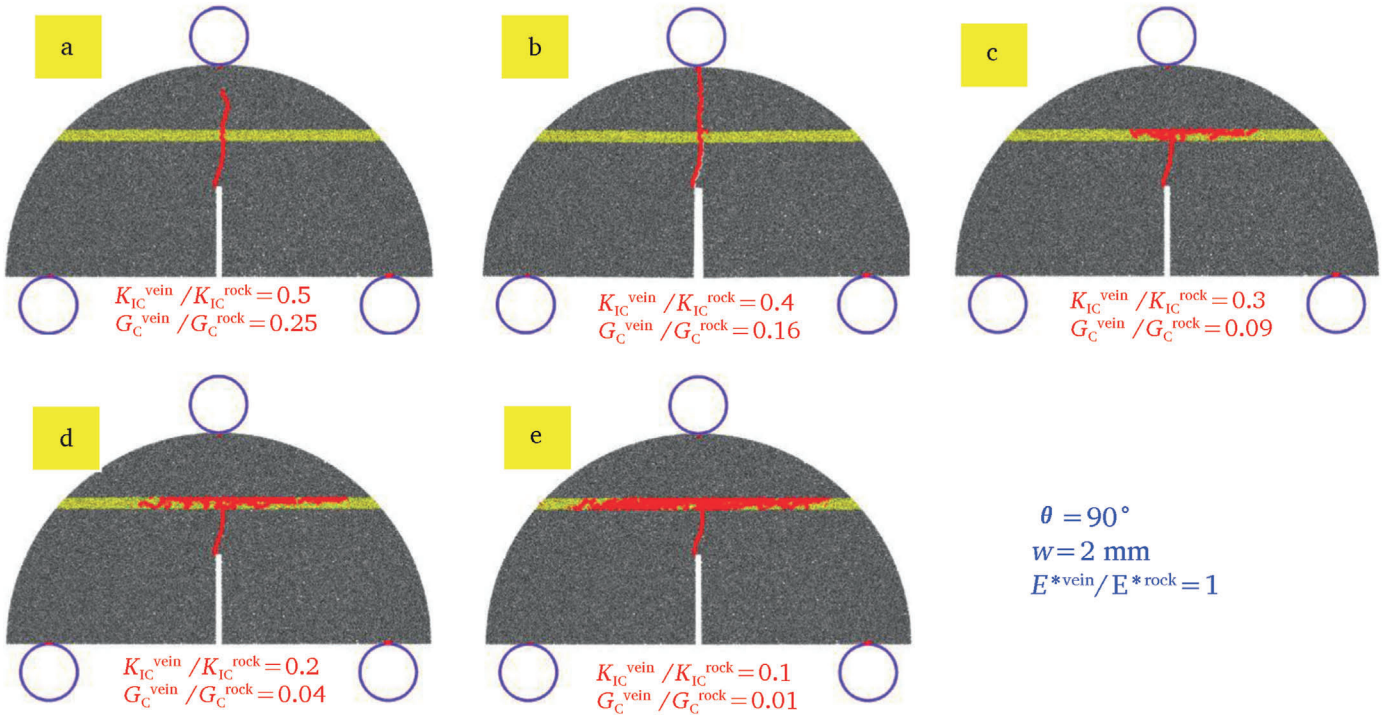

Fig. 8. Numerical test results of samples with vein ($\theta = 90°$, $w = 2$ mm, $1 \times E^{*rock}$) showing the influence of vein strength on the fracture diversion results. The five vein strengths of models are corresponding to (a) $0.5 \times K_{IC}^{rock}$, (b) $0.4 \times K_{IC}^{rock}$, (c) $0.3 \times K_{IC}^{rock}$, (d) $0.2 \times K_{IC}^{rock}$ and (e) $0.1 \times K_{IC}^{rock}$.

through the vein even before the fracture reached the vein. This is similar to the failure of weak or pre-damaged vein samples in the laboratory experiments. In a vein with higher stiffness, more micro-cracks are generated within the vein prior to the main fracture encountering it. In addition, the vein-parallel damage extended longer to the other direction at approach angle of −145° (Fig. 10d–i). Fig. 11 shows the number of micro-cracks and also the diversion distance during fracture propagation. When the vein stiffness $E^{*vein} = 0.5 \times E^{*rock}$, the number of fractures is 152 and the amount of fracture deflection distance is 4.86 mm. When the vein stiffness $E^{*vein} = 5 \times E^{*rock}$, the calculated number of fractures is 357 and the amount of fracture deflection distance is 15.95 mm. Fig. 11 shows that both the number of micro-cracks and the diversion distance exhibit a positive correlation with vein stiffness. In other words, higher vein stiffness results in more micro-cracks and a longer diversion distance.

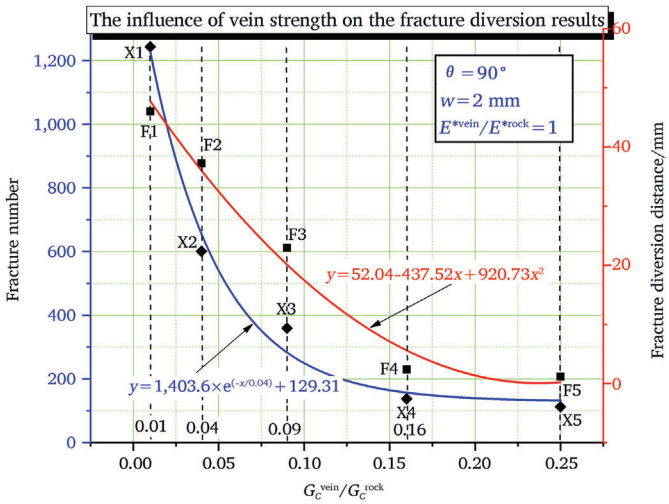

Fig. 9. The influence of vein strength on the fracture diversion distance and fracture number.

4.3. *Influence of approach angle on fracture path*

For all the tested SCB specimens with different bedding orientations in Table 2, both peak load and Mode-I fracture toughness increase with the bedding dip angle (Wang et al., 2017). Table 2 shows that 12 SCB specimens were tested for fracture toughness, with 11 specimens yielding valid results.

When $\theta = 0°$, that is, the loading direction is collinear with the bedding plane of the semi-round shale specimens (B1–B3), the average fracture toughness can be measured which is 0.655 MPa· $m^{1/2}$. When $\theta = 45°$, the mean value of fracture toughness of specimens (D1–D4) is 0.8 MPa· $m^{1/2}$. When $\theta = 90°$, that is, the loading direction is perpendicular to the bedding plane of the semi-round shale specimen (F1–F4), the mean fracture toughness can be measured as 0.83 MPa · $m^{1/2}$.

Figure 12 shows a boxplot graph of all SCB specimens fracture toughness values and the minimum and maximum fracture toughness of Mode-I specimens are 0.516 MPa· $m^{1/2}$ and 0.983 MPa· $m^{1/2}$. It can be seen from Fig. 12 which also presents the rock fracture surfaces in laboratory, that there exist great disparity in the fracture characteristics of specimens with different bedding orientations. The fracture path of shale specimen with horizontal or vertical bedding plane is approximately straight, but the fracture surface is rough and uneven. However, the fracture path of specimen with inclined bedding plane is approximately in the shape of a zigzag, and the fracture surface is much rougher. These SCB test results on the Marcellus Shale specimens also indicate that as the approach angle became more oblique to the propagating fracture, fracture diversion is more likely to occur (Lee et al., 2015).

In this section, six SCB discrete element numerical models were established to investigate the influence of different bedding plane dip angles on fracture propagation paths and its morphology. The bedding width w is 2 mm, the fracture toughness $K_{IC}^{vein}/K_{IC}^{rock}$ is 0.5, and the elastic modulus is $1.0 \times E^{*rock}$.

The dip angles of bedding plane were set to 15°, 30°, 45°, 60°, 75° and 90°, respectively. When the angle between the bedding and loading direction is in the range of 60° and 90°, the crack propagate across the bedding and barely deflect to the bedding (from Fig. 13a–c). When the

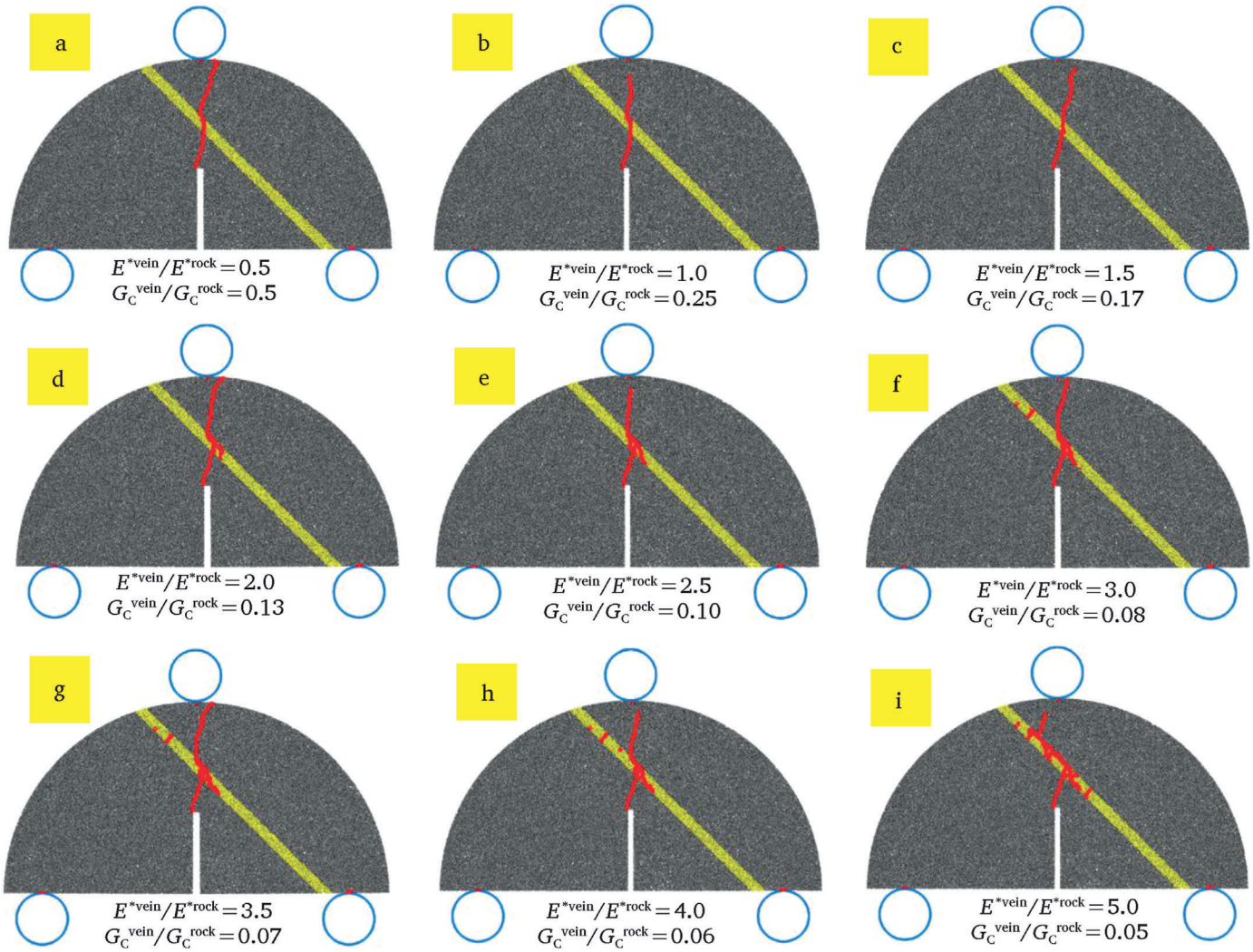

Fig. 10. Numerical test results of samples with vein ($\theta = 45°$, $w = 2$ mm, $K_{IC}^{vein}/K_{IC}^{rock} = 0.5$) showing the influence of vein stiffness on the fracture diversion results. The nine vein stiffnesses of models are corresponding to (a) 0.5 × E^{*rock}, (b) 1.0 × E^{*rock}, (c) 1.5 × E^{*rock}, (d) 2.0 × E^{*rock}, (e) 2.5 × E^{*rock}, (f) 3.0 × E^{*rock}, (g) 3.5 × E^{*rock}, (h) 4.0 × E^{*rock}, and (i) 5.0 × E^{*rock} respectively.

angle is less than 60°, the induced fractures first divert into the vein but kinks back into the rock matrix before reaching the end of the vein (from Fig. 13d–f). It can be observed that the induced fracture diverts into the vein but the fracture develops through the vein with a longer distance for the vein with a smaller approximation angle. This is similar to the failure of samples with weak or initially damaged vein in the laboratory experiments.

It is due to the fact that when the SCB specimen is subjected to indirect tensile load, the crack propagation is along the position where less strain energy is released. When the crack expands and intersects with the bedding plane, the propagation path mainly follows the bedding direction. However, sustained bedding-parallel propagation is impeded, causing the fracture to ultimately extend along the artificial notch toward the loading direction, forming an approximate saw tooth path.

4.4. Analysis and discussion

Hydraulic fracturing in naturally fractured reservoirs is a crucial for shale gas and shale oil development. The geometry of the resulting hydraulic fracture network in shale wells is largely determined by the interaction between hydraulic fractures and natural fractures (Gale et al., 2007). This study provides new insights into network complexity within reservoirs containing cemented natural fractures. Furthermore,

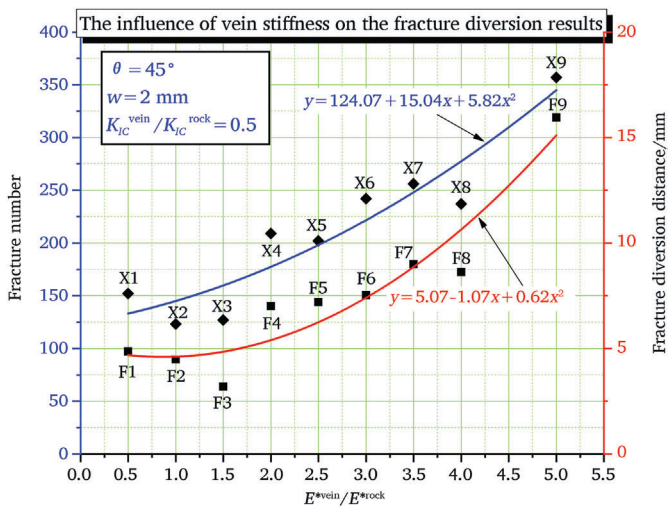

Fig. 11. The influence of vein stiffness on the fracture diversion distance and fracture number.

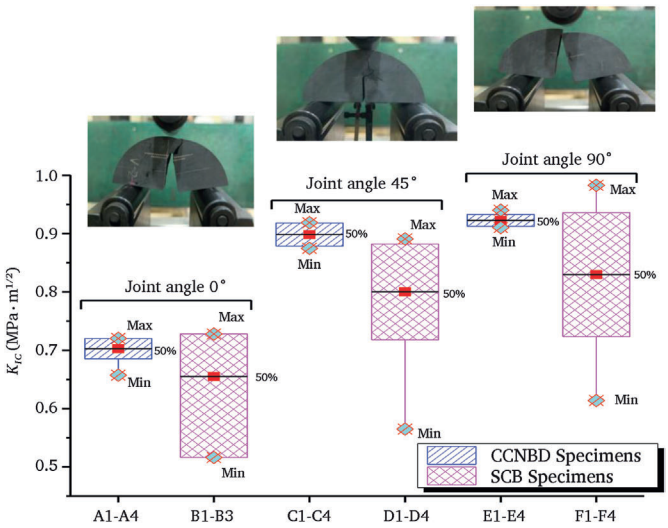

Fig. 12. Box-Chart plots of SCB fracture toughness values and photos of fracture surface (Wang et al., 2017).

the numerical results underscore the significance of characterizing natural fracture systems in the reservoir for achieving optimal stimulation. The rock's relative stiffness, strength, and critical energy release rate are determined not only by the pattern, size, and orientation of the natural fractures, but also by the type of vein-filling mineral. The rock matrix plays a vital role in predicting the reactivation of natural fractures during hydraulic fracturing treatments. Therefore, the results of fracture mechanics experiments and the corresponding discrete element numerical simulation of Mode-I SCB rspecimens can offer an intuitive, clear, and scientific approach to reveal artificial-natural fracture interaction mechanisms.

To investigate the influence of weak planes on hydraulic fracture propagation, Lee et al. (2015) performed semicircular bend tests on Marcellus Shale core samples with calcite-filled natural fractures (veins). Moreover, microscopic analyses of rock slices showed that induced fractures were deflected after encountering bedding, and the deflected fractures mainly expanded in bedding matrix (Hunjoo et al., 2018). Therefore, there are some kind of differences between the laboratory results and those simulated by the discrete element method in this study. In section 4 of the paper, the influences on the induced fracture propagation morphology are studied in regards of bedding strength, bedding stiffness and bedding angle. After induced fracture deflecting into bedding, induced fractures basically propagate predominantly along the interface between bedding and shale matrix, rather than within bedding matrix. This cause is that the influence of internal flaws and fluid inclusion trails on crack growth is not considered in the texture in the discrete element numerical calculation model. Therefore, the contact surface between the texture and shale is weaker and more prone to failure.

5. Conclusions

Based on the testing methods of fracture toughness and experimental results in reference (Wang et al., 2017), numerical simulation of cemented bedding fractures and fracture propagation path of shale specimens which occurs Mode-I fracture using discrete element method are performed, the following conclusions are drawn.

(1) Increasing parallel bond strength promotes fracture intersection. When the ratio of vein and shale fracture toughness is equal to 0.3, 0.2 and 0.1, that is to say, G_C^{vein}/G_C^{rock} is of 0.09, 0.04, 0.01, respectively, the opening mode fractures tend to divert and propagate a longer distance along the vein, forming extended steps.
(2) Higher vein stiffness increases fracture path complexity. When the vein stiffness is higher, the induced fractures divert into the vein and then propagate through the vein with a longer distance. The reason is that there generated much more micro-cracks inside the vein before the developing fracture encountered the vein. Morever, when the approach angle is −145°, the vein-parallel damage extends a longer distance to the other direction.
(3) When the angle between the bedding and the loading direction is in the range of 60° and 90°, the fracture spreads through the bedding and barely deflect to the bedding plane. When the angle

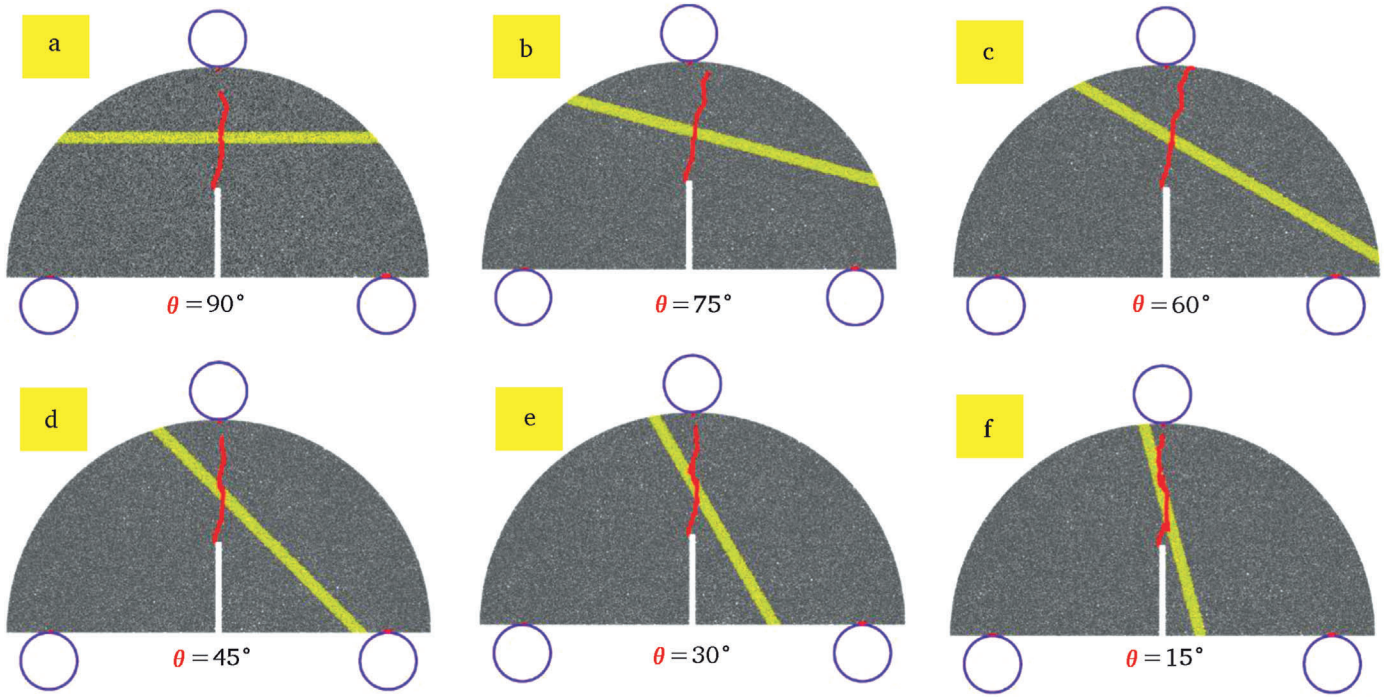

Fig. 13. SCB numerical test results of samples with vein (w = 2 mm, $K_{IC}^{vein}/K_{IC}^{rock}$ = 0.5, 1.0 × E^{*rock}) showing the influence of approach angle on fracture path.

between the bedding and the loading direction is less than 60°, the induced fractures firstly divert into the vein and then kinks back into the rock matrix before propagating to the end of the vein; This phenomenon is similar to the failure of weak or initially damaged vein samples in the laboratory experiments.

CRediT authorship contribution statement

Dubo Wang: Conceptualization. **Jinyu Dong:** Investigation. **Dongqiao Liu:** Data curation. **Xiangjun Chen:** Formal analysis. **Hai Zhong:** Data curation. **Mijia Yang:** Conceptualization. **Hongjian Wang:** Writing – review & editing, Writing – original draft.

Data availability

The datasets used and/or analyzed during the current study available from the corresponding author on reasonable request.

Acknowledgements

This research was funded by the Open Funding of State Key Laboratory of Intelligent Coal Mining and Strata Control (SKLIS202421), Henan Key Research and Development Program of China (No. 241111322900, 241111321100), Educational Research Program for Young and Middle-aged teachers of Fujian Province of China (JAT210425/B202106), Young Backbone Teachers of Undergraduate Colleges in Henan Province (2023GGJS077).

Declaration of competing interest

The authors declare that they have no known competing financial interests or personal relationships that could have appeared to influence the work reported in this paper.

List of symbols

E	Young's modulus of elasticity, GPa
E^*	Plain strain modulus of elasticity, GPa
ν	Poisson's ratio
K_{IC}	Mode-I fracture toughness
Y^*	Non-dimensional stress intensity factor
P	Applied load
B	Thickness of the specimen
D	Diameter of the specimen
Ds	Diameter of the saw
R	Radius of the specimen
h_c	Cutting depth
a	Length of the artificial notch
S	Distance between the two fulcrums
θ	Angle between the joints and the loading direction
β	a/R
G_C^{vein}	Vein fracture energy
G_C^{rock}	Rock fracture energy
SCB	Semi-Circular Bend

References

Amir, Y., Saeed, K., Hossein, J., 2024. Shear behavior and dilatancy of an artificial hard-matrix bimrock: an experimental study focusing on the role of blocky structure. Rock Mech. Bull. 3 (4), 100149.

Atkinson, B.K., 1989. Fracture Mechanics of Rock. Academic Press, London.

Barton, N., Choubey, V., 1977. The shear strength of rock joints in theory and practice. Rock Mech. 10 (1–2), 1–54.

Barton, N., Bandis, S., Bakhtar, K., 1985. Strength, deformation and conductivity coupling of rock joints. Int. J. Rock Mech. Min. Sci. Geomech. Abstr. 22 (3), 121–140.

Bell, F.G., Lindsay, P., 1999. The petrographic and geomechanical properties of some sandstones from the newspaper Member of the Natal Group near Durban, South Africa. Eng. Geol. 53 (1), 57–81.

Blanton, T.L., 1982. An Experimental Study of Interaction Between Hydraulically Induced and Pre-existing Fractures. SPE 10847.

Caox, M., Hirose, S., Sharmac, M.M., 2022. Factors controlling the formation of complex fracture networks in naturally fractured geothermal reservoirs. J. Pet. Sci. Eng. 208, 109642.

Chong, K.P., Kuruppu, M.D., 1984. New specimen for fracture toughness determination for rock and other materials. Inter. J. Frac. 26 (2), R59–R62.

Chuprakov, D.A., Akulich, A.V., Siebrits, E, Thiercelin, M., 2011. Hydraulic Fracture Propagation in a Naturally Fractured Reservoir. SPE 128715.

Chuprakov, D.A., Melchaeva, O., Prioul, R., 2013. Injection-sensitive mechanics of HF interaction with discontinuities. Rock Mech. Rock Eng. 47 (5), 1625–1640.

Dahi-Taleghani, A., Olson, J.E., 2009. Numerical modeling of multi-stranded hydraulic fracture propagation: accounting for the interaction between induced and natural fractures. SPE J. 16 (3), 575–581.

Damjanac, B., Cundall, P., 2016. Application of distinct element methods to simulation of hydraulic fracturing in naturally fractured reservoirs. Comput. Geotech. 71, 283–294.

Du, S.G., Lin, H., Yong, R., Liu, G.J., 2022. Characterization of joint roughness heterogeneity and its application in representative sample investigations. Rock Mech. Rock Eng. 55 (6), 3253–3277.

Fisher, M.K., Wright, C.A., Davidson, B.M., Steinsberger, N.P., Buckler, W.S., Goodwin, A., Fielder, E.O., 2005. Integrating fracture mapping technologies to improve stimulations in the Barnett shale. SPE Pro. Faci. 20 (2), 85–93.

Gale, J.F.W., Reed, R.M., Holder, J., 2007. Natural fractures in the Barnett shale and their importance for hydraulic fracture treatments. AAPG Bull. 91 (4), 603–622.

Gale, J.F.W., Laubach, S.E., Olson, J.E., Eichhubl, P., Fall, A., 2014. Natural fractures in shale: a review and new observations. AAPG Bull. 98 (11), 2165–2216.

Gao, G., Meguid, M.A., Chouinard, L.E., 2020. On the role of pre-existing discontinuities on the micromechanical behavior of confined rock samples: a numerical study. Acta Geotech. 15 (12), 3483–3510.

Gao, G., Meguid, M.A., Zhang, L., 2024. Exploring the role of sample size on fracture growth mechanisms in intact rock: insights from 3D DEM-DFN analysis. Can. Geotech. J. https://doi.org/10.1139/cgj-2023-0707.

He, Q., Suorineni, F., Oh, J., 2015. Modeling interaction between natural fractures and hydraulic fractures in block Cave mining. In: Proceedings of the 49th U.S. Rock Mech. Geomech. Symp. San Francisco, California, USA.

He, J.M., Li, T.F., Zheng, B., Mao, T.Q., Wu, Y.F., Li, S.D., Li, X., 2022a. Effect of calcite veins on the mechanical behavior and fracture propagation of carboniferous limestone. Eng. Geol. 300, 106592.

He, J.M., Lekan, O.A., Zheng, B., Mao, T.Q., Wu, Y.F., Li, G.F., Li, S.D., Li, X., 2022b. Effect of strain rate on anisotropic mechanical behavior of the shale under uniaxial compression conditions. Rock Mech. Rock Eng. 55, 5297–5305.

He, J.M., Zhang, Z.B., Li, G.F., Huo, J., Li, S.D., Li, X., 2022c. Modeling study on supercritical CO2 fracturing applicability and capacity to stimulate reservoirs with different permeabilities. J. Pet. Sci. Eng. 213, 110427.

Howarth, D.F., Rowlands, J.C., 1987. Quantitative assessment of rock texture and correlation with drill-ability and strength properties. Rock Mech. Rock Eng. 20 (1), 57–85.

Hunjoo, P.L., Jon, E.O., Richard, A.S., 2018. Interaction analysis of propagating opening mode fractures with veins using the Discrete Element Methodt. Int. J. Rock Mech. Min. Sci. 103, 275–288. https://doi.org/10.1016/j.ijrmms.2018.01.005.

ISRM Testing Commission, 1988. Suggested methods for determining the fracture toughness of rock. Int. J. Rock Mech. Min. Sci. Geomech. Abstr. 25 (2), 71–96.

ISRM Testing Commission, 1995. Suggested method for determining mode I fracture toughness using cracked chevron notched Brazilian disc (CCNBD) specimens. Int. J. Rock Mech. Min. Sci. Geomech. Abstr. 32 (1), 57–64.

Kolawole, O., Ispas, I., 2020. Interaction between hydraulic fractures and natural fractures: current status and prospective directions. J. Pet. Explor. Prod. Technol. 10, 1613–1634. https://doi.org/10.1007/s13202-019-00778-3.

Kulatilake, P., Malama, B., Wang, J., 2001. Physical and particle flow modeling of jointed rock block behavior under uniaxial loading. Int. J. Rock Mech. Min. Sci. 38 (5), 641–657.

Itasca Consulting Group Inc, 2015. PFC2D/3D (Particle Flow Code in 2/3 Dimensions). Version 5.0. ICG. Minneapolis, MN, USA.

Kuruppu, M.D., Obara, Y., Ayatollahi, M.R., Chong, K.P., Funatsu, T., 2015. ISRM-suggested method for determining the mode I static fracture toughness using semi-circular bend specimen. The ISRM Suggested Methods for Rock Characterization, Testing and Monitoring: 2007-2014. Springer International Publishing 107–114.

Laubach, S.E., 2003. Practical approaches to identifying sealed and open fractures. AAPG Bull. 87 (4), 561–579.

Lawn, B.R., Wilshaw, T.R., 1975. Fracture of Brittle Solids. Cambridge University Press.

Lee, H.P., Olson, J.E., Holder, J., Gale, J.F.W., Myers, R.D., 2015. The interaction of propagating opening mode fractures with preexisting discontinuities in shale. J. Geophy. Res. Solid Earth 120 (1), 169–181.

Lin, C., Jia, X., Deng, S., Mao, J., Chen, X., He, J., Li, X., 2024a. The roles of micro pores and minerals in shale during hydraulic fracturing. Rock Mech. Rock Eng. https://doi.org/10.1007/s00603-024-04063-6.

Lin, C., Deng, S., Mao, J., Jiang, Z., Chen, X., Yang, X., Zhang, Y., He, J., Li, Y., Zheng, C., 2024b. A new brittleness evaluation index for Reservoir rocks based on fuzzy analytic hierarchy process and energy dissipation. SPE J. https://doi.org/10.2118/223083-PA.

Maxwell, S.C., Urbancic, T.I., Steinsberger, N., Zinno, R., 2002. Microseismic imaging of hydraulic fracture complexity in the Barnett Shale. In: Proceedings of the SPE Annual Technical Conference and Exhibition, SPE-77440-MS. San Antonio, Texas, USA.

Mteiri, S.A., Suboyin, A., Rahman, M.M., Haroun, M., 2021. Hydraulic fracture propagation and analysis in heterogeneous Middle Eastern tight gas reservoirs: influence of natural fractures and well placement. ACS Omega 6 (1), 799–815. https://doi.org/10.1021/acsomega.0c05380.

Osiptsov, A.A., 2017. Fluid mechanics of hydraulic fracturing: a review. J. Pet. Sci. Eng. 156, 513–535.

Potyondy, D.O., 2015. The bonded-particle model as a tool for rock mechanics research and application: current trends and future directions. Geosyst. Eng. 18 (1), 1–28. https://doi.org/10.1080/12269328.2014.998346.

Potyondy, D.O., Cundall, P.A., 2004. A bonded-particle model for rock. Int. J. Rock Mech. Min. Sci. 41 (1), 329–364.

Renshaw, C.E., Pollard, D.D., 1995. An experimentally verified criterion for propagation across unbonded frictional interfaces in brittle,linear elastic materials. Int. J. Rock Mech. Min. Sci. Geomech. Abstr. 32 (3), 237–249.

Tang, Z.C., Zhang, Z.F., Zhao, L.C., Xiao, S.G., 2025. A microscopic DEM investigation on fracture shearing characteristics of infilled grains with different geometrical shapes in rock discontinuities. Rock Mech. Bull. 4 (2), 100174.

Wang, Q.Z., Jia, X.M., Wu, L.Z., 2004. Wide-range stress intensity factors for the ISRM suggested method using CCNBD specimens for rock fracture toughness tests. Inter. J. Rock Mech. Min. Sci. 41 (4), 709–716.

Wang, H.J., Liu, D.A., Cui, Z.D., Cheng, C., Jian, Z., 2016. Investigation of the fracture modes of red sandstone using XFEM and acoustic emissions. Theor. Appl. Fract. Mech. 85, 283–293.

Wang, H.J., Zhao, F., Huang, Z.Q., Yao, Y.M., Yuan, G.X., 2017. Experimental Study of Mode-I fracture toughness for layered shale based on two ISRM-Suggested methods. Rock Mech. Rock Eng. 50 (7), 1933–1939.

Wang, W.W., Jon, E.O., Maša, P., Richard, A.S., 2018. Interaction between cemented natural fractures and hydraulic fractures assessed by experiments and numerical simulations. J. Pet. Sci. Eng. 167, 506–516. https://doi.org/10.1016/j.petrol.2018.03.095.

Warpinski, N.R., Teufel, L.W., 1987. Influence of geologic discontinuities on hydraulic fracture propagation. J. Pet. Tech. 39 (2), 209–220.

Wu, K., Olson, J., 2014. Mechanics analysis of interaction between hydraulic and natural fractures in shale reservoirs. Unconventional Resources Technology Conference, Denver, Colorado, 25-27 August 2014. Society of Exploration Geophysicists, American Association of Petroleum Geologists, Society of Petroleum Engineers, pp. 1824–1841.

Wu, R., Kresse, O., Weng, X., Cohen, C., Gu, H., 2012. Modeling of Interaction of Hydraulic Fractures in Complex Fracture Networks. SPE 152052.

Zhang, X., Thiercelin, M.J., Jeffrey, R.G., 2007. Effects of Frictional Geological Discontinuities on Hydraulic Fracture Propagation. SPE 106111.

Zhao, Z.J., Wang, H.J., Cui, Z.D., Zhao, F., Tang, T.W., Han, W.G., Wang, X.D., 2021. Experimental study on Mode-I fracture toughness using Chevron Straight-notched semi-circular Bend (CSNSCB) method. Theor. Appl. Fract. Mech. 116, 103093. https://doi.org/10.1016/j.tafmec.2021.103093.